




Shallow-water hydrothermal venting linked to the Palaeocene–Eocene Thermal Maximum

Received: 23 April 2022

Accepted: 4 July 2023

Published online: 03 August 2023

 Check for updates

Christian Berndt ¹✉, Sverre Planke ^{2,3}, Carlos A. Alvarez Zarikian ⁴, Joost Frieling ⁵, Morgan T. Jones ³, John M. Millett ^{2,6}, Henk Brinkhuis ⁷, Stefan Bünz ⁸, Henrik H. Svensen³, Jack Longman ^{9,10}, Reed P. Scherer ¹¹, Jens Karstens ¹, Ben Manton ², Mei Nelissen ⁷, Brandon Reed¹¹, Jan Inge Faleide ³, Ritske S. Huismans ¹², Amar Agarwal ¹³, Graham D. M. Andrews ¹⁴, Peter Betlem ^{3,15}, Joyeeta Bhattacharya¹⁶, Sayantani Chatterjee ^{17,18}, Marialena Christopoulou¹¹, Vincent J. Clementi ¹⁹, Eric C. Ferré ²⁰, Irina Y. Filina ²¹, Pengyuan Guo ²², Dustin T. Harper²³, Sarah Lambert ²³, Geoffroy Mohn ²⁴, Reina Nakaoka²⁵, Christian Tegner ²⁶, Natalia Varela ²⁷, Mengyuan Wang ²⁸, Weimu Xu ²⁹ & Stacy L. Yager³⁰

The Palaeocene–Eocene Thermal Maximum (PETM) was a global warming event of 5–6 °C around 56 million years ago caused by input of carbon into the ocean and atmosphere. Hydrothermal venting of greenhouse gases produced in contact aureoles surrounding magmatic intrusions in the North Atlantic Igneous Province have been proposed to play a key role in the PETM carbon-cycle perturbation, but the precise timing, magnitude and climatic impact of such venting remains uncertain. Here we present seismic data and the results of a five-borehole transect sampling the crater of a hydrothermal vent complex in the Northeast Atlantic. Stable carbon isotope stratigraphy and dinoflagellate cyst biostratigraphy reveal a negative carbon isotope excursion coincident with the appearance of the index taxon *Apectodinium augustum* in the vent crater, firmly tying the infill to the PETM. The shape of the crater and stratified sediments suggests large-scale explosive gas release during the initial phase of vent formation followed by rapid, but largely undisturbed, diatomite-rich infill. Moreover, we show that these vents erupted in very shallow water across the North Atlantic Igneous Province, such that volatile emissions would have entered the atmosphere almost directly without oxidation to CO₂ and at the onset of the PETM.

The Palaeocene–Eocene Thermal Maximum (PETM)^{1,2} was a period of transiently elevated global temperatures marking the earliest Eocene (~56 million years before present (Ma)) that lasted for ~200,000 years^{3,4} and had a profound influence on the global climate and ecosystems^{5,6}. The PETM is of particular interest because it provides an example

from the geological record with multiple similarities to present-day global warming associated with anthropogenic greenhouse gas emissions. Multi-proxy analysis of globally distributed sediment cores has shown that global surface temperatures rose by 5–6 °C during the PETM onset^{2,7}, exceeding even the worst-case Intergovernmental

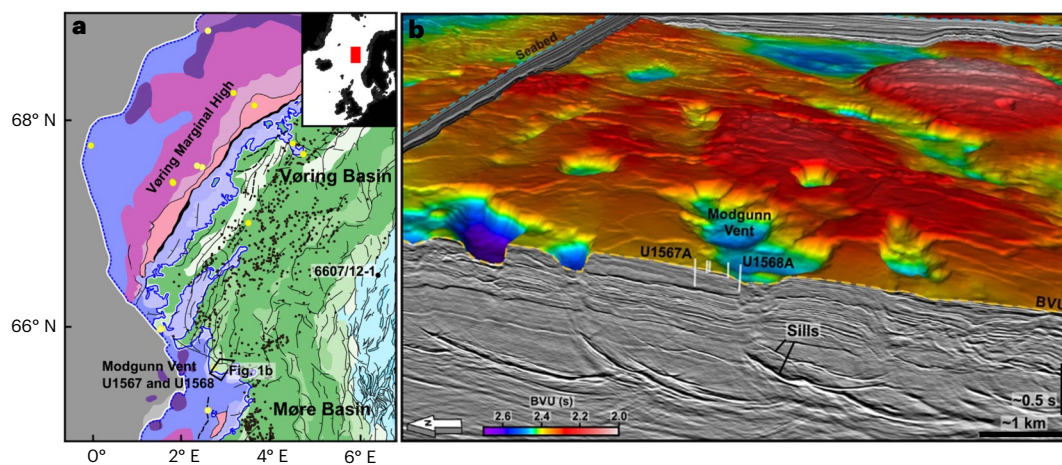


Fig. 1 | HTVCs on the mid-Norwegian margin. **a**, Structural elements⁴⁶. Purple colours, extrusive volcanic elements related to continental break-up; green colours, Cretaceous basins; black dots, hydrothermal vents; grey, oceanic crust. Yellow dots, Deep Sea Drilling Project, Ocean Drilling Project and Integrated Ocean Discovery Program drill sites. For complete legend, see ref. 46.

Inset shows location of study area. **b**, Three-dimensional view of seismic reflection data showing the relationship between volcanic intrusions (sills) and the palaeoseafloor depressions formed by the hydrothermal venting. BVU, interpreted Base Vent Unconformity. Industry 3D seismic data courtesy of TGS under a Creative Commons license CC BY 4.0.

Panel on Climate Change representative concentration pathway 8.5 scenario for temperature rise over the next few centuries⁸. The PETM is globally associated with a -2% to -7% carbon isotope excursion (CIE)⁹. The CIE onset was relatively rapid, followed by a plateau and protracted recovery period⁹. Mass-balance calculations indicate that the CIE onset was caused by the injection of up to 12,000 gigatons (Gt) of ^{13}C -depleted carbon over a geologically rapid time frame of only a few thousand years^{10,11}.

The widespread emplacement of magmatic intrusions into sedimentary basins during the formation of the North Atlantic Igneous Province (NAIP) around 56 Ma has been implicated as a potential carbon source for instigating the PETM^{2,12} (Fig. 1). Sill intrusions would have rapidly volatilized organic matter in surrounding sediments, transporting, among others, CH_4 and CO_2 to the surface by hydrothermal and explosive activity^{13,14}. Geophysical observations show more than 700 potential hydrothermal vent complexes (HTVCs) on the mid-Norwegian margin alone¹², and observations from other basins with less extensive seismic coverage such as the East Greenland margin indicate that they were also affected by sill intrusions and hydrothermal venting¹⁵. Detailed seismic interpretations placed the majority of the HTVCs close to the Palaeocene–Eocene palaeosurface¹⁶, hinting at a temporal correlation between thermogenic degassing and PETM hyperthermal conditions. Sill–sediment interactions are common features in continental large igneous provinces, and several studies have invoked thermogenic degassing as the cause of warming and extinction events associated with other large igneous provinces in the geological record^{13,17,18}. Although the hypothesis that contact metamorphism of sedimentary basins could cause major environmental disturbances has gained substantial traction in recent years, definitive confirmation on the basis of field localities and precise geochronological records was lacking. Even in the comparatively recent NAIP, only a single borehole had previously been drilled into an HTVC, but it was not cored. The 20 samples from around the vent base in this borehole (6607/12-1) appear to show that this vent was active during the PETM CIE¹⁹. However, these well-cutting samples cannot be used to precisely determine the formation time of the HTVC; because of fall-in, there is significant uncertainty from which depth in the borehole materials derive. The water depths at which these vents formed and emitted carbon into the water column is crucial to the resulting atmospheric CH_4 and CO_2 fluxes. A shallow-water or subaerial vent will release gaseous carbon directly into the atmosphere, leading to less oxidation of methane

via volatile–water interactions, thus enhancing short-term (decadal) atmospheric warming, as CH_4 has a much more powerful greenhouse effect than CO_2 (ref. 18). Therefore, further coring of NAIP HTVCs is required to assess the role of thermogenic degassing on the Palaeocene–Eocene carbon cycle, to provide a more precise age control and constrain the palaeowater depths that these vents erupted at.

Rapid HTVC formation and infill

High-resolution three-dimensional (3D) seismic data document a shallow HTVC on the Modgunn Arch offshore Norway, a location less than 10 km from the rift axis of the Møre Margin (Fig. 1a). The HTVC consists of an approximately 400-m-deep and 200- to 240-m-wide feeder system that extends vertically from a sill complex at the bottom to a funnel-shaped seafloor crater at the top (Fig. 1b). The sill complex consists of several interconnected intrusions that extend at least 5 km laterally and that are probably several tens of metres thick, given their very high seismic amplitudes in the exploration 3D seismic data (Fig. 1b). The Modgunn Vent crater is approximately 80 m deep with respect to the surrounding palaeoseafloor. The seismic data show two styles of crater infill (Fig. 2). First, there are infilling strata that dip towards the centre of the vent, either draping or downlapping at the bottom and truncated at the top by an erosional unconformity. Second, there is a doming of these reflections in the central part of the vent. The dome is covered by onlapping reflections, suggesting mobilization and uplift of the crater infill after deposition. The seismically incoherent feeder system and the funnel-shaped seafloor depression are typical for HTVCs on the Norwegian Margin^{12,16,20,21}. Similar feeder systems have been described in outcrops in the Karoo Basin (South Africa), where they consist of fragmented sedimentary rocks altered due to fluid migration and high temperatures¹³. The funnel shape and aspect ratio of the Modgunn Vent crater is similar to diatreme-crater systems in maar volcanoes^{22,23} and blow-out craters due to drilling accidents^{24–26} (Extended Data Fig. 1), indicating rapid initial formation by fluid overpressure release. The continuous nature of the infilling strata in most of the crater suggests undisturbed sedimentation and limited fluid migration after formation, as opposed to fluid escape systems that have been active for thousands of years²⁷.

International Ocean Discovery Program (IODP) Expedition 396²⁸ drilled five boreholes up to 200 m below the seafloor and through the crater infill in the Modgunn Vent (U1567A–C and U1568A and B). The boreholes are situated along a 500-m-long transect from the crater

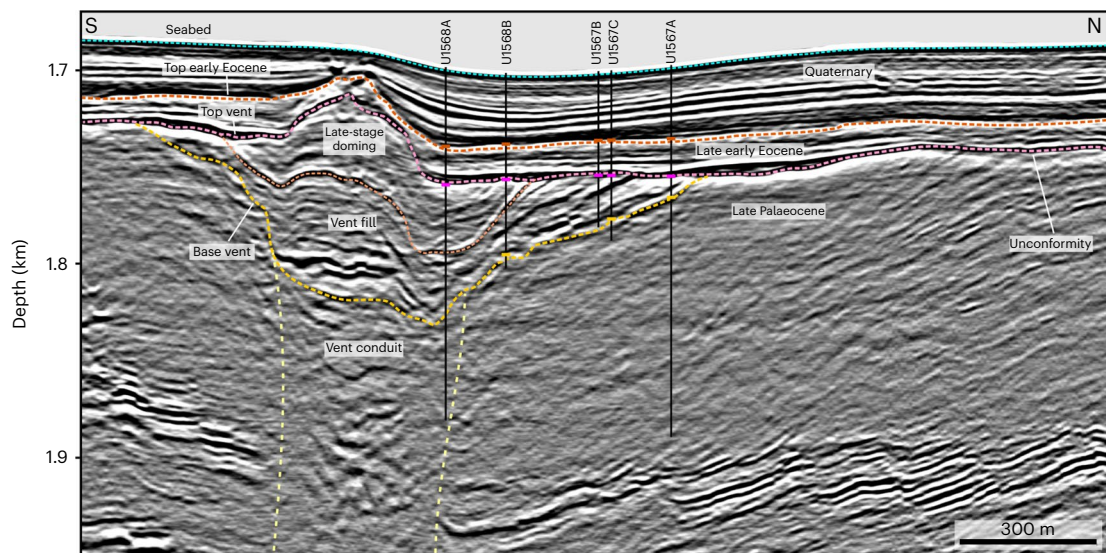


Fig. 2 | Interpreted high-resolution 3D seismic image of the Modgunn Vent showing the location of the five boreholes. Note the unconformity that forms the top vent reflection, indicating shallow water depth shortly after vent filling. Onlap relationships on the vent fill between the top vent and base vent horizons document doming after the unconformity was formed. Black lines indicate the

intervals penetrated by IODP Expedition 396 boreholes. Coloured markers on the boreholes indicate formation tops: orange, top early Eocene; magenta, top vent; dark yellow, top Palaeocene; light yellow, approximate vent conduit limit. Seismic data were depth converted, with $1,600 \text{ m s}^{-1}$ corresponding to average P-wave velocity measured in the boreholes.

rim to almost the centre of the vent next to the dome structure (Fig. 2). This unique drilling profile recorded high sediment core recovery (303.35 m or 82.9% and 239.37 m or 91.83% for sites U1567 and U1568, respectively), allowing detailed and unparalleled characterization of the crater infill. The infill consists of two lithological units (IV and V) dominantly comprising very dark grey to black diatomite. Ubiquitous ash layers are present throughout the vent fill, attesting to the common occurrence of surface or shallow-water volcanism during this period²⁹ (Fig. 3). The boreholes of the sites U1567 and U1568 did not penetrate any hyaloclastite deposits or intrusive magmatic rocks. The Palaeocene and PETM sections of U1567, in the outer peripheral part of the vent fill, include well-preserved laminated diatomite, whereas the thicker mudstone sequence of U1568, proximal to the vent dome, is characterized by diagenetically altered ash-rich diatomite with much poorer siliceous microfossil preservation. We do not observe evidence for alteration by high-temperature fluids in the recovered sedimentary record. However, operational safety precautions prevented drilling at the centre of the vent, and such signatures, if present, could be confined to the central and deeper parts of the crater that we were not allowed to drill. Core catchers collected within the vent infill (lithological units IV and V; Fig. 3) yielded the dinoflagellate cyst (dinocyst) PETM-marker taxon *Apectodinium augustum*³⁰. For the same samples, stable carbon isotope analyses of bulk organic matter ($\delta^{13}\text{C}_{\text{org}}$) show a characteristic negative CIE of -2% compared with the underlying strata, documenting in situ infill of the crater following the onset of the PETM³¹ (Supplementary Fig. 1). The presence of graded ash beds and sub-millimetre-scale laminated (altered) diatomite all suggest rapid and largely undisturbed infill consistent with the seismic observations.

Timing of HTVC formation

The greenish mudstones below the crater infill (Unit VI) contain the dinoflagellate cyst (dinocyst) taxon *Alisocysta margarita*, giving a late Palaeocene age for the host rock sediments in which the vent formed. Stable carbon isotope analyses of bulk organic matter ($\delta^{13}\text{C}_{\text{org}}$) from Unit VI samples show steady values of -25.8% (Fig. 3). Analysed samples from lithological Unit IV and upper part of Unit V (Fig. 3) yielded the dinocyst PETM-marker taxon *Apectodinium augustum*³⁰ (Extended Data Tables 1–4). The first occurrence and consistent appearance of

the diatom *Hemiaulus proteus* in these strata further supports a PETM age³². The lowermost samples of Unit V, which are also interpreted as vent infill, show continued stable $\delta^{13}\text{C}_{\text{org}}$ values matching those in Unit VI and do not contain PETM-marker taxa. Around 10–15 m above the base vent in boreholes U1567B and U1567C is an -6% drop in $\delta^{13}\text{C}_{\text{org}}$, marking the PETM CIE onset. Upwards, this is followed by a more moderate (-2%) negative excursion compared with the underlying pre-PETM strata, documenting further infill of the crater following the onset of the PETM³¹ (Fig. 3 and Extended Data Fig. 2). The overall CIE shape appears to be influenced by a switch from predominantly marine to terrestrial sedimentary organic matter that was observed directly above the most negative $\delta^{13}\text{C}_{\text{org}}$ values (Fig. 3). Palaeocene–Eocene terrestrial and marine organic matter are -4% offset³³, whereby, in contrast to present day, marine organic matter is more ^{13}C -depleted compared with terrestrial organic matter³⁴. When compared with age-equivalent samples with similar organic matter characteristics, it is clear that both the terrestrial and marine organic matter-dominated samples show $\delta^{13}\text{C}_{\text{org}}$ values most consistent with those previously observed for the PETM CIE body³³ (Supplementary Information and Extended Data Fig. 2). The shape of the CIE also matches that observed in a core from the northern North Sea³⁵, the closest studied section to the Modgunn locality. The recovery phase of the CIE appears to be absent at the Modgunn sites, and we therefore argue that the vent formation occurred just before the onset of the PETM CIE and that the crater infill occurred throughout the latest Palaeocene and earliest phases of the PETM.

The erosional unconformity that forms the top of the vent infill is overlain by lithological Unit III, which consists of dark grey to brownish mudstones with concomitant occurrences of the dinocyst taxa *Glaphyrocysta ordinata*, *Hystriochosphaeridium tubiferum* and *Deflandrea oebisfeldensis*, and infrequent *Membranilarnacia compressa* (Supplementary Information). This assemblage indicates a middle early Eocene ($<50 \text{ Ma}$) age for the unconformity and the sediments onlapping onto the dome structure³⁶, implying that the Unit IV to Unit III erosional unconformity corresponds to a hiatus of $>5 \text{ Myr}$. The seismic onlap relationship of the sediments above the unconformity and the dome structure furthermore indicate that remobilization and uplift of some of the crater infill occurred within $\sim 5 \text{ Myr}$ after the crater was infilled.

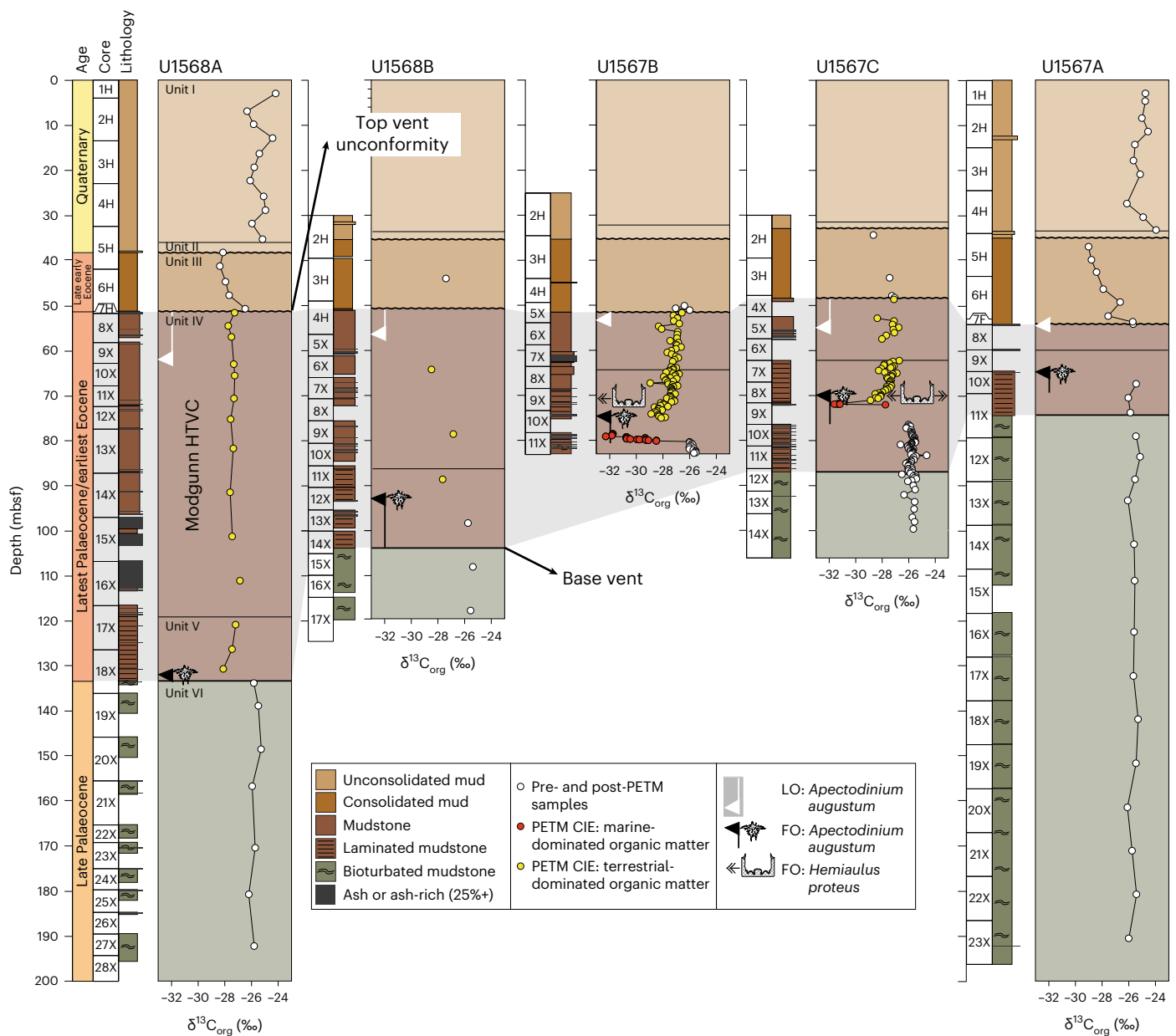


Fig. 3 | IODP Expedition 396 borehole information showing the late Palaeocene and early PETM fill (lithostratigraphic units IV and V). From left to right, proximity to the centre of the HTVC decreases. The grey background delineates the Modgunn Vent infill. The ‘unconformity’ label indicates the unconformity that formed shortly after the vent; other unconformities are indicated by wiggly lines. The $\delta^{13}\text{C}$ measurements were carried out on total

organic carbon ($\delta^{13}\text{C}_{\text{org}}$). Red dots indicate the onset of the PETM CIE dominated by marine organic matter, and yellow dots indicate the PETM CIE with organic material largely derived from terrestrial sources. Biostratigraphic dating is discussed in the text and the electronic supplement. mbsf, metres below seafloor according to IODP’s C-SFA definition; LO, last occurrence; FO, first occurrence.

A shallow-water carbon source

The high-resolution 3D seismic data document the extent of the erosional unconformity that truncates the top of the vent infill and the host rock in its vicinity (Fig. 2). The unconformity is present throughout most of the high-resolution 3D seismic cube coverage, but it is more difficult to discern in the lower-frequency exploration 3D seismic data that cover the entire region (Fig. 1b). Nevertheless, regional conventional 3D seismic data show that the unconformity is present within an approximately 20 by 30 km wide area on the Modgunn Arch at the transition between the Vøring and Møre basins. Although deep marine erosion may form unconformities in exceptional oceanographic settings³⁷, the fact that the unconformity on Modgunn Arch is laterally extensive and formed in a marginal basin is direct evidence

for a shallow-water or even a short-lived subaerial setting during the earliest early Eocene.

The inferred shallow-water depth of the Modgunn HTVC is supported by the distinctly coastal marine palynological and diatom assemblages in the vent infill. Organic microfossils are overwhelmingly dominated by terrestrial elements (pollen, spores, heterogeneous transported land plant materials, alongside dinocysts with coastal to restricted marine to coastal ecological affinities such as *Glaphyrocysta*, *Hystrichosphaeridium*, *Cerodinium*, *Senegalinium* and *Deflandrea* spp.³⁸) of lithological units IV and V (vent infill). The diatom assemblage that accumulated in the crater is dominantly coastal marine, neritic and typified by abundant and diverse *Hemiaulus* spp. as well as *Scoptronis*, *Syndropsis* and *Grunoviella* spp., which are often associated

with benthic or floating macroalgae³⁹. There is ample evidence for (near-) coastal conditions, but we find no evidence for sedimentary redistribution by wave action, constraining the water depth inside the crater ring to below wave base, often assumed ≥ 30 metres (ref. 40).

Implications for PETM origin

The observation that the Modgunn Vent formed under shallow marine conditions implies that its impact on climate was significantly greater than if it had formed in the deep sea. Magmatic intrusion-related hydrothermal systems release both CO₂ and CH₄ (ref. 41), but for submerged systems, it is well documented that the water column acts as an efficient filter for CH₄ as most is oxidized to CO₂ in the water column before reaching the atmosphere⁴². While on decadal–centennial timescales CH₄ is 25 times more potent a greenhouse gas than CO₂, its atmospheric residence time is short (~9 years), after which it is oxidized to CO₂⁴³. Therefore, direct and rapid addition of CH₄ to the atmosphere results in greater initial warming and has a greater impact on climate and surface carbon feedback processes than does carbon emitted as CO₂⁴⁴. Thus, the original CH₄/CO₂ ratio in HTVC volatiles, the rate of CH₄ and CO₂ venting and water depth are all highly relevant for the climatic effects of hydrothermal venting⁴⁵.

Although we do not constrain the overall amount or the speciation of the carbon that was emitted by NAIP-related sill emplacement beyond the estimates by Svensen et al.¹², our findings provide direct evidence that widespread HTVCs erupted in very shallow marine settings of the northern North Atlantic region around the time of the PETM. The characteristic CIE as recorded in $\delta^{13}\text{C}_{\text{org}}$ appears to be positioned within the rapidly deposited vent infill but above the crater base. As this is observed in several, but crucially not all, boreholes in the transect, it is most likely that the studied vent formed just before the onset of the PETM and refilled during the onset and body of the CIE. The high-resolution C-isotope curve from Site U1567C places the CIE onset 11–15 m above the vent base (Fig. 2), which paired with exceptionally high sediment and ash accumulation rates indicate that the vent formed probably only a few millennia before the PETM onset (Supplementary Information). Notably, the stratigraphic record of this early infill is missing near the centre of the HTVC (U1568A) (Fig. 3), which could imply sediments could not accumulate there until around millennia after crater formation due to ongoing hydrothermal activity and/or slumping into the (active) crater centre.

The shallow marine setting allowed for efficient injection of methane and other volatiles into the atmosphere at the time of formation. The Modgunn Arch is close to the ocean–continent boundary and therefore among the HTVCs on the mid-Norwegian margin that are closest to the rift axis, suggesting that many other vents were in equally shallow water or even above sea level at this time. This is supported by similar shallow near-coastal conditions reconstructed using palynological analyses of the cuttings obtained from the only other HTVC that has so far been drilled on the Norwegian Margin (well 6607/12-1; refs. 12, 19). The direct and rapid injection of large volumes of hydrothermal gases, including methane, into the atmosphere at this time increases the potential impact of hydrothermal venting on global climate. Most important, our constraints on both the timing and environment of venting in the Northeast Atlantic are conclusive evidence for hydrothermal venting immediately before the PETM onset, and therefore it probably played a major role in driving hyperthermal conditions.

Online content

Any methods, additional references, Nature Portfolio reporting summaries, source data, extended data, supplementary information, acknowledgements, peer review information; details of author contributions and competing interests; and statements of data and code availability are available at <https://doi.org/10.1038/s41561-023-01246-8>.

References

- Kennett, J. P. & Stott, L. D. Abrupt deep-sea warming, palaeoceanographic changes and benthic extinctions at the end of the Palaeocene. *Nature* **353**, 225–229 (1991).
- Frieling, J. et al. Extreme warmth and heat-stressed plankton in the tropics during the Paleocene–Eocene Thermal Maximum. *Sci. Adv.* **3**, e1600891 (2017).
- Jones, T. D. et al. Dynamics of sediment flux to a bathyal continental margin section through the Paleocene–Eocene Thermal Maximum. *Clim. Past* **14**, 1035–1049 (2018).
- Murphy, B. H., Farley, K. A. & Zachos, J. C. An extraterrestrial ³He-based timescale for the Paleocene–Eocene Thermal Maximum (PETM) from Walvis Ridge, IODP Site 1266. *Geochim. Cosmochim. Acta* **74**, 5098–5108 (2010).
- Sluijs, A. et al. Warming, euxinia and sea level rise during the Paleocene–Eocene Thermal Maximum on the Gulf Coastal Plain: implications for ocean oxygenation and nutrient cycling. *Clim. Past* **10**, 1421–1439 (2014).
- Carmichael, M. J. et al. Hydrological and associated biogeochemical consequences of rapid global warming during the Paleocene–Eocene Thermal Maximum. *Glob. Planet. Change* **157**, 114–138 (2017).
- Inglis, G. N. et al. Global mean surface temperature and climate sensitivity of the early Eocene Climatic Optimum (EECO), Paleocene–Eocene Thermal Maximum (PETM), and latest Paleocene. *Clim. Past* **16**, 1953–1968 (2020).
- Burke, K. D. et al. Pliocene and Eocene provide best analogs for near-future climates. *Proc. Natl Acad. Sci. USA* **115**, 201809600 (2018).
- McInerney, F. A. & Wing, S. L. The Paleocene–Eocene Thermal Maximum: a perturbation of carbon cycle, climate, and biosphere with implications for the future. *Annu. Rev. Earth Planet. Sci.* **39**, 489–516 (2011).
- Zeebe, R. E., Ridgwell, A. & Zachos, J. C. Anthropogenic carbon release rate unprecedented during the past 66 million years. *Nat. Geosci.* **9**, 325–329 (2016).
- Turner, S. K. & Ridgwell, A. Development of a novel empirical framework for interpreting geological carbon isotope excursions, with implications for the rate of carbon injection across the PETM. *Earth Planet. Sci. Lett.* **435**, 1–13 (2016).
- Svensen, H. et al. Release of methane from a volcanic basin as a mechanism for initial Eocene global warming. *Nature* **429**, 542–545 (2004).
- Svensen, H., Jamtveit, B., Planke, S. & Chevallier, L. Structure and evolution of hydrothermal vent complexes in the Karoo Basin, South Africa. *J. Geol. Soc.* **163**, 671–682 (2006).
- Iyer, K., Schmid, D. W., Planke, S. & Millett, J. Modelling hydrothermal venting in volcanic sedimentary basins: impact on hydrocarbon maturation and paleoclimate. *Earth Planet. Sci. Lett.* **467**, 30–42 (2017).
- Reynolds, P. et al. Hydrothermal vent complexes offshore Northeast Greenland: a potential role in driving the PETM. *Earth Planet. Sci. Lett.* **467**, 72–78 (2017).
- Planke, S., Rasmussen, T., Rey, S. S. & Myklebust, R. Seismic characteristics and distribution of volcanic intrusions and hydrothermal vent complexes in the Vøring and Møre basins. In *Petroleum Geology: North-West Europe and Global Perspectives—Proceedings of the 6th Petroleum Geology Conference* (eds Dore, A. G. & Vining, B. A.) 833–844 (Geological Society, 2005).
- Burgess, S. D., Muirhead, J. D. & Bowring, S. A. Initial pulse of Siberian Traps sills as the trigger of the end-Permian mass extinction. *Nat. Commun.* **8**, 164 (2017).
- Tian, X. & Buck, W. R. Intrusions induce global warming before continental flood basalt volcanism. *Nat. Geosci.* **15**, 417–422 (2022).

19. Frieling, J. et al. Thermogenic methane release as a cause for the long duration of the PETM. *Proc. Natl Acad. Sci. USA* <https://doi.org/10.1073/pnas.1603348113> (2016).
20. Svensen, H., Planke, S., Jamtveit, B. & Pedersen, T. Seep carbonate formation controlled by hydrothermal vent complexes: a case study from the Vøring Basin, the Norwegian Sea. *Geo Mar. Lett.* **23**, 351–358 (2003).
21. Kjøberg, S. et al. 3D structure and formation of hydrothermal vent complexes at the Paleocene–Eocene transition, the Møre Basin, mid-Norwegian margin. *Interpretation* **5**, SK65–SK81 (2017).
22. Lorenz, V. & Kurszlaukis, S. Root zone processes in the phreatomagmatic pipe emplacement model and consequences for the evolution of maar–diatreme volcanoes. *J. Volcanol. Geothermal Res.* **159**, 4–32 (2007).
23. White, J. D. L. & Ross, P.-S. Maar–diatreme volcanoes: a review. *J. Volcanol. Geothermal Res.* **201**, 1–29 (2011).
24. Thatje, S., Gerdes, D. & Rachor, E. A seafloor crater in the German Bight and its effects on the benthos. *Helgol. Mar. Res.* **53**, 36–44 (1999).
25. Leifer, I. & Judd, A. The UK22/4b blowout 20 years on: investigations of continuing methane emissions from sub-seabed to the atmosphere in a North Sea context. *Mar. Pet. Geol.* **68**, 706–717 (2015).
26. Karstens, J. et al. Formation of the Figge Maar seafloor crater during the 1964 B1 blowout in the German North Sea. *Earth Sci. Syst. Soc.* **2**, 10053 (2022).
27. Böttner, C. et al. Pockmarks in the Witch Ground Basin, Central North Sea. *Geochem. Geophys. Geosyst.* **20**, 1698–1719 (2019).
28. Planke, S., Berndt, C., Zarijian, C. A. A. & The Expedition 396 Scientists Expedition 396 Preliminary Report: Mid-Norwegian Continental Margin Magmatism (IODP, 2022); <https://doi.org/10.14379/iodp.pr.396.2022>
29. Stokke, E. W., Liu, E. J. & Jones, M. T. Evidence of explosive hydromagmatic eruptions during the emplacement of the North Atlantic Igneous Province. *Volcanica* **3**, 227–250 (2020).
30. Crouch, E. M. et al. Global dinoflagellate event associated with the late Paleocene thermal maximum. *Geology* **29**, 315–318 (2001).
31. Sluijs, A. et al. Subtropical Arctic Ocean temperatures during the Palaeocene/Eocene thermal maximum. *Nature* **441**, 610–613 (2006).
32. Oreshkina, T. V. & Radionova, E. P. Diatom record of the Paleocene–Eocene Thermal Maximum in marine paleobasins of Central Russia, Transuralia and adjacent regions. *Nova Hedwig. Beih.* **143**, 307–336 (2014).
33. Sluijs, A. & Dickens, G. R. Assessing offsets between the $\delta^{13}\text{C}$ of sedimentary components and the global exogenic carbon pool across early Paleogene carbon cycle perturbations. *Glob. Biogeochem Cycles* **26**, GB4005 (2012); <https://doi.org/10.1029/2011GB004224>
34. Hayes, J. M., Strauss, H. & Kaufman, A. J. The abundance of ^{13}C in marine organic matter and isotopic fractionation in the global biogeochemical cycle of carbon during the past 800 Ma. *Chem. Geol.* **161**, 103–125 (1999).
35. Jones, M. T. et al. Mercury anomalies across the Palaeocene–Eocene Thermal Maximum. *Clim. Past* **15**, 217–236 (2019).
36. Bujak, J. & Mudge, D. A high-resolution North Sea Eocene dinocyst zonation. *J. Geol. Soc. Lond.* **151**, 449–462 (1994).
37. Das, P. et al. Deep-sea submarine erosion by the Kuroshio Current in the Manila accretionary prism, offshore Southern Taiwan. *Tectonophysics* **807**, 228813 (2021).
38. Frieling, J. & Sluijs, S. Towards quantitative environmental reconstructions from ancient non-analogue microfossil assemblages: ecological preferences of Paleocene–Eocene dinoflagellates. *Earth Sci. Rev.* **185**, 956–973 (2018).
39. Round, F. E., Crawford, R. M. & Mann, D. G. *The Diatoms: Biology and Morphology of the Genera* (Cambridge Univ. Press, 1990).
40. Peters, S. E. & Loss, D. P. Storm and fair-weather wave base: a relevant distinction? *Geology* **40**, 511–514 (2012).
41. Berndt, C. et al. Rifting under steam—how rift magmatism triggers methane venting from sedimentary basins. *Geology* **44**, 767–770 (2016).
42. Naudts, L. et al. Geological and morphological setting of 2778 methane seeps in the Dnepr paleo-delta, northwestern Black Sea. *Mar. Geol.* **227**, 177–199 (2006).
43. Schaefer, H. On the causes and consequences of recent trends in atmospheric methane. *Curr. Clim. Change Rep.* **5**, 259–274 (2019).
44. Reinhard, C. T. et al. Oceanic and atmospheric methane cycling in the cGENIE Earth system model—release v0.9.14. *Geosci. Model Dev.* **13**, 5687–5706 (2020).
45. Gutjahr, M. et al. Very large release of mostly volcanic carbon during the Palaeocene–Eocene Thermal Maximum. *Nat. Publ. Group* **548**, 573–577 (2017).
46. Gernigon, L. et al. A digital compilation of structural and magmatic elements of the Mid-Norwegian continental margin. *Nor. J. Geol.* **101**, 202112 (2021); <https://doi.org/10.17850/njg101-3-2>

Publisher's note Springer Nature remains neutral with regard to jurisdictional claims in published maps and institutional affiliations.

Open Access This article is licensed under a Creative Commons Attribution 4.0 International License, which permits use, sharing, adaptation, distribution and reproduction in any medium or format, as long as you give appropriate credit to the original author(s) and the source, provide a link to the Creative Commons license, and indicate if changes were made. The images or other third party material in this article are included in the article's Creative Commons license, unless indicated otherwise in a credit line to the material. If material is not included in the article's Creative Commons license and your intended use is not permitted by statutory regulation or exceeds the permitted use, you will need to obtain permission directly from the copyright holder. To view a copy of this license, visit <http://creativecommons.org/licenses/by/4.0/>.

© The Author(s) 2023

¹GEOMAR Helmholtz Centre for Ocean Research Kiel, Kiel, Germany. ²Volcanic Basin Energy Research AS, Høienhald, Oslo, Norway. ³Department of Geosciences, University of Oslo, Oslo, Norway. ⁴International Ocean Discovery Program, Texas A&M University, College Station, TX, USA. ⁵Department of Earth Sciences, University of Oxford, Oxford, UK. ⁶Department of Geology and Geophysics, University of Aberdeen, King's College, Aberdeen, UK. ⁷NIOZ Royal Netherlands Institute for Sea Research, Den Burg, Texel, the Netherlands. ⁸Department of Geology, UiT The Arctic University of Tromsø, Tromsø, Norway. ⁹Marine Isotope Geochemistry, Institute for Chemistry and Biology of the Marine Environment (ICBM), University of Oldenburg, Oldenburg, Germany. ¹⁰Department of Geography and Environmental Sciences, Northumbria University, Newcastle-upon-Tyne, UK. ¹¹Department of Earth, Atmosphere and Environment, Northern Illinois University, DeKalb, IL, USA. ¹²Department of Earth Science, University of Bergen, Bergen, Norway. ¹³Applied Structural Geology, Department of Earth Sciences, Indian Institute of Technology Kanpur, Kanpur, India. ¹⁴School of Environmental Sciences Faculty of Science and Engineering, University of Hull, Hull, UK. ¹⁵Department of Arctic Geology, The University Centre in Svalbard, Svalbard, Norway. ¹⁶Picarro Inc., Santa Clara, CA, USA. ¹⁷Department of Geology, Niigata University, Niigata, Japan. ¹⁸Earthquake Research Institute, The University of Tokyo, Tokyo, Japan. ¹⁹Department of Marine and Coastal Sciences, Rutgers University, New Brunswick, NJ, USA. ²⁰School of Geoscience, University of Louisiana

at Lafayette, Lafayette, LA, USA. ²¹Department of Earth and Atmospheric Sciences, University of Nebraska, Lincoln, NE, USA. ²²Institute of Oceanology, Chinese Academy of Sciences, Qingdao, China. ²³Department of Geology and Geophysics, University of Utah, Salt Lake City, UT, USA. ²⁴Laboratoire Géosciences et Environnement Cergy (GEC), CY Cergy Paris Université, Neuville sur Oise, France. ²⁵Department of Planetology, Kobe University, Kobe, Japan. ²⁶Department of Geoscience, Aarhus University, Aarhus C, Denmark. ²⁷Department of Geosciences, Virginia Tech, Blacksburg, VA, USA. ²⁸School of Marine Sciences, Sun Yat-sen University, Zhuhai, China. ²⁹School of Earth Sciences and the SFI Research Centre in Applied Geosciences (iCrag), University College Dublin, Dublin, Ireland. ³⁰Department of Environment, Geology, and Natural Resources, Ball State University, Muncie, IN, USA.

✉ e-mail: cberndt@geomar.de

Methods

Seismic processing and interpretation

The high-resolution 3D seismic data were acquired in summer 2020 on board the Norwegian RV *Helmer Hanssen* using the P-Cable system⁴⁷. This system consists of fourteen 25-m-long hydrophone cables spaced 12.5 m apart perpendicular to the ship's steaming direction⁴⁸. Each hydrophone cable contains eight receiver groups with a group interval of 3.125 m. Two mini-GI airguns with a total volume of 90 inch³ provided seismic energy with high frequency and relatively large bandwidth (20–400 Hz) at a shot interval of 6 s. The dominant frequency of the seismic data is at 170–180 Hz. The 3D seismic data were processed applying a standard, well-established processing sequence^{48,49}. The sequence consists of removal of bad channels, geometry assignment, tide static and residual static corrections, compensation for amplitude loss (spherical divergence), de-ghosting in the pre-stack domain, band-pass filter, 3D binning at 6.25 × 6.25 m and normal moveout correction, mean stack, 3D spatial filtering to further reduce noise and 3D Stolt migration using a constant average water velocity. Seismic interpretation used the commercially available KingdomSuite seismic and geological interpretation software from S&P Global⁵⁰ and the Petrel software from Schlumberger⁵¹. All five boreholes (U1567A–C and U1568A and B) at Modgunn Vent were integrated with the 3D seismic data to identify key stratigraphic marker horizons Top Palaeocene and Top early Eocene as well as vent infill and the top vent unconformity using the P-wave velocities measured on the cores and within the boreholes.

Biostratigraphy

For most pre-Quaternary core-catcher samples from holes U1567A ($n = 21$), U1567B ($n = 9$), U1568A ($n = 25$) and additional samples from U1568B ($n = 2$), approximately 5–10 cm³ (~10 g) of sediment was taken for palynological processing with strong acids (HCl and HF). Shipboard processing followed a shortened version of standard palynological laboratory protocols⁵². Samples were first soaked in a small volume (~5 ml) of 10% HCl to dissolve minor amounts of carbonate before addition of a larger volume (~25 ml) of 38–40% HF to partly dissolve silicates, all in 50 ml plastic centrifuge tubes. After cold HF digestion on a vortex shaker for ~2–4 h, samples were centrifuged at ~3,200 rotations per minute to separate the residue from HF and facilitate decanting the supernatant. Subsequently, the residues were treated twice with 30–35% HCl to remove any silica gels that may have formed and finally rinsed twice with demineralized water to neutralize any remaining acids. After each of these steps, samples were centrifuged, and supernatants were decanted. The residues were then sieved to remove large and small organic and residual mineral particles using 250 µm and 15 µm nylon sieves and an ultrasonic bath. The fraction between 15 and 250 µm was concentrated again using a centrifuge and mounted on glass microscope slides using glycerine jelly as the mounting medium and finally sealed with nail varnish for more permanent conservation. Each slide was entirely analysed for age-diagnostic species^{36,53} using a Zeiss transmitted light microscope at ×100–400 magnification and, when sample quality permitted, for a broad description of the palynofacies.

Shipboard analysis of biosiliceous microfossils was largely from smear slides using Zeiss transmitted light microscopy at ×630 and ×1,000 magnification, with selected samples sieved at 15 µm after disaggregation with 15% H₂O₂. Post-expedition analyses followed the slide preparation method of Warnock and Scherer⁵⁴. Analysis of in situ diatomite laminations was carried out on board using a Hitachi TM-3000 scanning electron microscope. Further details on the biostratigraphic analysis are provided in the Supplementary Information.

Carbon isotopes

The total organic carbon (TOC) and stable carbon isotope ratios ($\delta^{13}\text{C}_{\text{org}}$) of each sample were determined by powdering and

decalcifying using 1 M HCl for 72 h. The samples were oven dried at 50 °C and re-homogenized. Between 5 and 15 mg of decalcified sample was transferred to tin capsules and loaded into a Costech Analytical Zero-Blank Autosampler. The $\delta^{13}\text{C}_{\text{org}}$ measurements and TOC concentrations were analysed using a Thermo Fisher Scientific Flash Elemental Analyzer, coupled to a Thermo Fisher Scientific DeltaV Isotope Ratio Mass Spectrometer at the CLIPT Lab, University of Oslo. Each sample was run in duplicate to test reproducibility, which was <0.06‰ and <0.01 wt% for $\delta^{13}\text{C}_{\text{org}}$ and TOC, respectively.

Data availability

All data are freely available through the IODP data base (<https://web.iodp.tamu.edu/LORE>) except for the industry 3D seismic data (AMN17) shown in Fig. 1. For access, contact TGS, Oslo (Reidun.Myklebust@tgs.com). Source data are provided with this paper.

References

- Planke, S., Erikson, F. N., Berndt, C., Mienert, J. & Masson, D. P-cable high-resolution seismic. *Oceanography* **22**, 85 (2009).
- Waage, M., Bünz, S., Landrø, M., Plaza-Flaverola, A. & Waghorn, K. A. Repeatability of high-resolution 3D seismic data. *Geophysics* <https://doi.org/10.1190/geo2018-0099.1> (2019).
- Waghorn, K. A., Bünz, S., Plaza-Faverola, A. & Johnson, J. E. 3-D seismic investigation of a gas hydrate and fluid flow system on an active mid-ocean ridge; Svyatogor Ridge, Fram Strait. *Geochem. Geophys. Geosyst.* **19**, 2325–2341 (2018).
- KingdomSuite v.2021 (S&P Global, 2021).
- Petrel v.2019.1 (Schlumberger, 2019).
- Brinkhuis, H. et al. Late Eocene–Quaternary dinoflagellate cysts from ODP Site 1168, off western Tasmania. In *Proc. ODP, Sci. Results* Vol. 189 (eds Exxon, N. F., Kennett, J. P. & Malone, M. J.) 1–36 (Texas A & M Univ., 2003); http://www-odp.tamu.edu/publications/189_SR/VOLUME/CHAPTERS/105.PDF
- Vieira, M. & Mahdi, S. New Paleocene species and biostratigraphic relevance of the genus *Spiniferites* across the North Sea and Norwegian Sea. *Rev. Paleobot. Palynol.* **262**, 28–43 (2019).
- Warnock, J. P. & Scherer, R. P. A revised method for determining the absolute abundance of diatoms. *J. Paleolimnol.* **53**, 157–163 (2015).

Acknowledgements

The work was funded through the Integrated Ocean Drilling Program. We thank the master, crew and technical staff of D/S *Joides Resolution* on Expedition 396. Without their efforts, this work would not have been possible. S.P., M.T.J., H.H.S. and J.I.F. acknowledge the support of the Research Council of Norway through the PALMAR (no. 336293) and CEED (no. 223272) research projects. The other authors were funded through IODP for Expedition 396. We thank the Norwegian Petroleum Directorate and AkerBP (PDRILL project) for supporting site survey acquisition and data analyses, and TGS for access to seismic data.

Author contributions

C.B., S.P., J.M.M., J.F., C.T., J.I.F., R.S.H., M.T.J., H.H.S. and S.B. designed the study. H.B., J.F., R.P.S., M.N. and B.R. conducted the biostratigraphic analysis. J.K. and B.M. did the seismic analysis. J.L. and M.T.J. did the geochemical analysis. S.P., C.B., C.A.A.Z., G.D.M.A., A.A., P.B., J.B., H.B., S.C., M.C., V.J.C., E.C.F., I.Y.F., J.F., P.G., D.T.H., M.T.J., S.L., J.L., J.M.M., G.M., R.N., R.P.S., C.T., N.V., M.W., W.X. and S.L.Y. collected the borehole data during IODP Expedition 396. All authors wrote the manuscript.

Funding

Open access funding provided by GEOMAR Helmholtz-Zentrum für Ozeanforschung Kiel.

Competing interests

The authors declare no competing interests.

Additional information

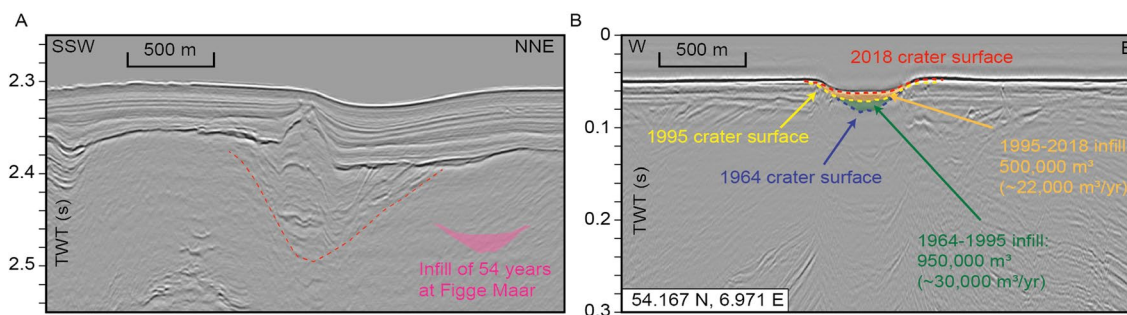
Extended data is available for this paper at <https://doi.org/10.1038/s41561-023-01246-8>.

Supplementary information The online version contains supplementary material available at <https://doi.org/10.1038/s41561-023-01246-8>.

Correspondence and requests for materials should be addressed to Christian Berndt.

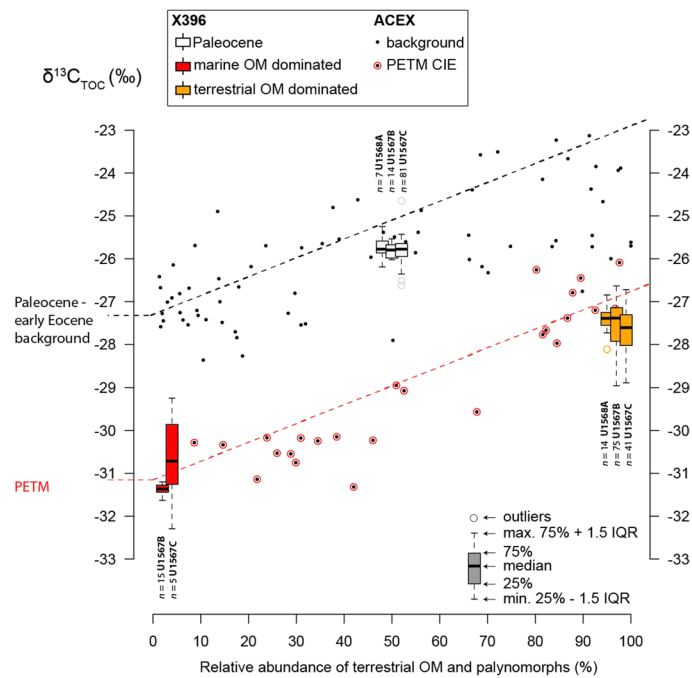
Peer review information *Nature Geoscience* thanks Andy Ridgwell, John Hopper and the other, anonymous, reviewer(s) for their contribution to the peer review of this work. Primary Handling Editor: James Super, in collaboration with the *Nature Geoscience* team.

Reprints and permissions information is available at www.nature.com/reprints.



Extended Data Fig. 1 | Same-scale comparison of seismic reflection profiles of the Modgunn Vent crater and the Figge Maar blow-out crater in the German North Sea. **a.** Seismic reflection profile of the Modgunn Vent crater with its base marked by a red dashed line and down-lapping seismic reflections indicate episodic infill of the crater originally ~80 m deep. **b.** Seismic reflection profile of the Figge Maar crater with time-converted bathymetric grids from 1995 and 2018 and an original crater floor reconstruction from 1964 revealing the rapid infill of up to 25 m of sediments within a period of only 54 years. The refilling of the 37 m-deep Figge Maar blow-out crater in the southern North Sea demonstrates how quickly eruption induced seafloor depressions can be refilled and may

serve as a partial analogue for the Modgunn Vent (Thatje et al., 1999). For the Figge Maar blow-out crater, the strong currents in a shallow water sediment-rich environment provided enough material to fill much of the depression within half a century. Although these conditions imply the Figge Maar infill was likely far more rapid than could be the case for the Modgunn Vent crater, the depositional geometries are very similar to those indicated by seismic reflections within the Modgunn Vent crater. The similar seismic geometries suggest that the crater formed rapidly and some of the material displaced during crater formation may have provided the lowermost crater infill.



Extended Data Fig. 2 | $\delta^{13}\text{C}_{\text{org}}$ values from previously published PETM and Early Eocene strata relative to terrestrial palynomorph abundance (Arctic Coring Expedition (ACEX), Site M0004a. The black (background) line represents the organic matter source mixing line as determined in Sluijs & Dickens³³. This line (in ‰) takes the form of $ax + b = 0.044 \times \text{terrestrial pollen} (\%) - 27.3$. The PETM mixing line is 3.9‰ offset from the Paleocene–Eocene background, reflecting the approximate size of the PETM CIE³³. To facilitate

comparison with the new isotope data, ACEX data flagged as ‘PETM CIE’ are limited to the interval where *Apectodinium augustum* occurs consistently³¹. The Paleocene samples of Unit VI and V (Holes U1568A, U1567B and U1567C) are shown as box-whisker plots (white) and were determined to contain approximately equal proportions of marine and terrestrial organic matter (~50%). The marine-dominated samples (U1567B and U1567C; red box plots) show the expected -4‰ CIE previously reconstructed for the ACEX samples³³.

Extended Data Table 1 | Occurrence of dinoflagellate cysts and age assessment at Sites 1567A

U1567A									
Site	Hole	Core	Section	bottom (cm in section)	top (cm in section)	CSF-A Depth top (m)	CSF-A mid depth (m)	Age	Bujak & Mudge Zone
U1567	A	3	CC	21	17	24.65	24.67	Quaternary	-
U1567	A	4	CC	34	29	35.21	35.235	Quaternary	-
U1567	A	5	CC	5	0	43.08	43.105	late Early Eocene	E3
U1567	A	6	CC	26	23	53.39	53.405	late Early Eocene	E3
U1567	A	7	CC	18	13	53.99	54.015	-	-
U1567	A	8	CC	19	17	54.27	54.28	-	-
U1567	A	9	CC	19	13	59.83	59.86	PETM	P6b
U1567	A	10	CC	20	15	70.46	70.485		
U1567	A	11	CC	36	31	78.98	79.005	latest Paleocene	tentative P6a
U1567	A	12	CC	27	19	88.53	88.57		
U1567	A	13	CC	21	16	98.38	98.405		
U1567	A	14	CC	24	19	108.23	108.255		
U1567	A	15	CC	14	9	111.83	111.855		
U1567	A	16	CC	24	19	127.35	127.375	Late Paleocene	P5b
U1567	A	17	CC	21	16	137.36	137.385	Late Paleocene	P5b
U1567	A	18	CC	31	26	147.08	147.105		
U1567	A	19	CC	19	14	156.81	156.835		
U1567	A	20	CC	39	34	166.82	166.845		
U1567	A	21	CC	38	33	176.49	176.515		
U1567	A	22	CC	36	31	186.1	186.125		
U1567	A	23	CC	36	31	195.96	195.985		

Detailed information is available in the digital supplement SI Paly supp. U1567-U1568.xlsx.

Extended Data Table 2 | Occurrence of dinoflagellate cysts and age assessment at Sites 1567B

U1567B									
Site	Hole	Core	Section	bottom (cm in section)	top (cm in section)	CSF-A Depth top (m)	CSF-A mid depth (m)	Age	Bujak & Mudge Zone
U1567	B	3	CC	20	15	44.2	44.225	late Early Eocene	E3
U1567	B	4	CC	23	18	49.24	49.265	barren	-
U1567	B	5	CC	22	17	53.88	53.905	PETM	P6b
U1567	B	6	CC	42	41	58.86	58.865	PETM	P6b
U1567	B	7	CC	29	28	62.49	62.495	PETM	P6b
U1567	B	8	CC	26	27	68.74	68.735	PETM	P6b
U1567	B	9	CC	22	21	73.48	73.485	PETM	P6b
U1567	B	10	CC	37	36	75.1	75.105	PETM	P6b
U1567	B	11	CC	26	25	82.87	82.875	latest Paleocene	P6a

Detailed information is available in the digital supplement SI Paly supp. U1567-U1568.xlsx.

Extended Data Table 3 | Occurrence of dinoflagellate cysts and age assessment at Sites 1568A

U1568A								
Site	Hole	Core	Section	bottom (cm in section)	top (cm in section)	CSF-A mid depth (m)	Age	Bujak & Mudge Zone
U1568	A	3	CC	10	5	23.155	Quaternary	
U1568	A	4	CC	30	25	32.815	Quaternary	
U1568	A	5	CC	26	21	42.285	Barren	
U1568	A	7	CC	30	25	51.675	earliest Eocene	E1
U1568	A	8	CC	37	32	57.105	Barren	
U1568	A	9	CC	39	34	63.155	~Barren	
U1568	A	10	CC	47	42	68.175	PETM	P6b
U1568	A	11	CC	29	24	72.155	PETM	P6b
U1568	A	12	CC	22	17	77.235	PETM	P6b
U1568	A	13	CC	31	26	87.095	PETM	P6b
U1568	A	14	CC	40	35	96.435	PETM	P6b
U1568	A	15	CC	46	41	103.675	PETM	P6b
U1568	A	16	CC	44	39	113.355	-	
U1568	A	17	CC	39	34	126.455	PETM	P6b
U1568	A	18	CC	33	28	133.945	Late Paleocene	P5b
U1568	A	19	CC	37	32	140.395	Late Paleocene	P5b
U1568	A	20	CC	39	34	149.945	Late Paleocene	P5b
U1568	A	21	CC	57	52	158.505	Late Paleocene	P5a/b
U1568	A	22	CC	32	27	168.155	Late Paleocene	P5a/b
U1568	A	23	CC	21	16	171.485	Late Paleocene	P5a/b
U1568	A	24	CC	24	17	178.055	Late Paleocene	P5a/b
U1568	A	25	CC	23	18	181.855	Late Paleocene	P5a/b
U1568	A	26	CC	22	19	184.905	Late Paleocene	P5a/b
U1568	A	27	CC	47	42	194.565	Late Paleocene	P5a/b
U1568	A	28	CC	40	35	195.565	Late Paleocene	P5a/b

Detailed information is available in the digital supplement SI Paly supp. U1567-U1568.xlsx.

Extended Data Table 4 | Occurrence of dinoflagellate cysts and age assessment at Sites 1568B

U1568B								
Site	Hole	Core	Section	bottom (cm in section)	top (cm in section)	CSF-A mid depth (m)	Age	<u>Bujak & Mudge Zone</u>
U1568	B	4	2W	68	69	51.185	late Early Eocene	E3
U1568	B	14	CC	36	35	105.405	latest <u>Paleocene</u>	tentative P6a

Detailed information is available in the digital supplement SI Paly supp. U1567-U1568.xlsx.